# 國 立 交 通 大 學

## 光電工程研究所
## 碩 士 論 文

氧化鋅量子點中不受激發功率影響之激子態研究

Invariable exciton states upon increasing

pumping in ZnO quantum dots

研 究 生：廖婉君

指導教授：謝文峰　教授

張振雄　教授

中 華 民 國 九 十 九 年 六 月

氧化鋅量子點中不受激發功率影響之激子態研究

# Invariable exciton states upon increasing pumping in ZnO quantum dots

研 究 生：廖婉君        Student: Wan-Jiun Liao

指導老師：謝文峰　教授     Advisors: Dr. Wen-Feng Hsieh

         張振雄　教授          Dr. Chen-Shiung Chang

國立交通大學

光電工程研究所

碩士論文

A Thesis

Submitted to Institute of Electro-Optical Engineering

College of Electrical Engineering and Computer Science

National Chiao Tung University

In partial Fulfillment of the Requirements

for the Degree of

Master

in

Electro-Optical Engineering

June 2010

Hsinchu, Taiwan, Republic of China

中 華 民 國 九 十 九 年 六 月

# Invariable exciton states upon increasing pumping in ZnO quantum dots
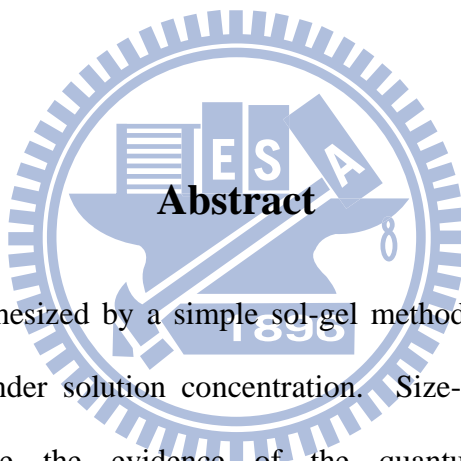
Student: Wan-Jiun Liao          Advisor: Dr. Wen-Feng Hsieh

Dr. Chen-Shiung Chang

Department of Photonics & Institute of Electro-Optical Engineering

National Chiao Tung University

## Abstract

ZnO QDs are synthesized by a simple sol-gel method and the average size of QDs can be tailored under solution concentration. Size-dependent blue shifts of photoluminescence give the evidence of the quantum confinement effect. Furthermore, the unchanged spectral profiles of near-bandedge emission (NBE) for a fixed size of ZnO quantum dots (QDs) reveal no signature of biexciton formation and exciton-exciton scattering under excitation density covering three orders of magnitude. These results quite differ from that of the micrometer-sized powder. The intensities of NBE peaks attributed to free exciton and surface bound exciton states exhibit linear dependence on the excitation power density that confirms the invariable exciton states with no effect of two-exciton interaction in ZnO QDs upon increasing the pump intensity.

# 氧化鋅量子點中不受激發功率影響之激子態研究

研究生：廖婉君　　　　　　　　　指導老師：謝文峰　教授

張振雄　教授

國立交通大學光電工程研究所

## 摘要

利用溶膠–凝膠法藉由改變溶液濃度來合成不同晶粒大小的氧化鋅量子點，並量測其光學特性。從低溫螢光光譜隨氧化鋅量子點尺寸變小而藍移的現象可觀察到在氧化鋅量子點中存在量子侷限效應。然而，量測變功率螢光光譜發現，當激發光強度改變了1000倍，除了光譜強度會隨激發強度增加而變大外，NBE的光譜形狀幾乎都不變，且觀察不到雙激子的形成與激子與激子的散射現象，此情形與氧化鋅塊材的特性相當不一樣。另外，自由激子與表面束縛激子的發光能量幾乎不隨激發光強度改變及線性的發光強度與激發能量關係，表示當激發功率增加，仍沒有激子間的交互作用，因此在氧化鋅量子點中，存在穩定的激子態。

# 誌謝

時間過得真快，一轉眼我的碩士生生活就要結束了。在這兩年的日子裡，我學習與成長了很多，也讓我的想法與處事態度變得更成熟了。

研究所這段期間，我要謝謝我的指導教授謝文峰老師，謝謝老師在課業、研究與待人處事上對我的指導與教誨，以及對我在生活上的關心，從老師的身上我學習到很多。也要謝謝另外一位指導教授張振雄老師，提供我專業意見，以及生活上的幫助。接下來要謝謝小豪帶我入門做實驗，雖然我常做出讓你啞口無言的事，不過真的很謝謝你教了我很多事。還要謝謝小郭，當我研究上有問題時，常常向你請教，謝謝你提供我很多想法與協助。也要謝謝楊松幫我打XRD與教我SEM。以及謝謝鄭信民學長對我研究的關心與協助，還有歐博濟，雖然在碩二之後才跟你比較有交集，常向你請教TRPL的問題，你也常會關心我的近況，論文或找工作的進展如何，謝謝你。另外，智章學長、維仁學長、碧軒學長以及黃董偶爾我有問題要請教你們，你們也都很熱心的幫我解答，謝謝你們。還有要謝謝黃至賢，很多生活上的瑣碎事情常會去煩你，謝謝你啦，實驗室有了你讓我很不無聊了XD

另外，謝謝蔡智雅學姐，課業上或是找工作等常找你幫忙或詢問你意見，謝謝你；還要謝謝陳厚仁總是很大方的借我筆記與考古題，祝你跟學姐永遠甜蜜幸福喔XD 還有黃冠智，常常會以你的經驗告訴我很多事情以及提供我建議，以及林建輝，你真是一個奇妙的人，你的很多事情與想法常讓我們驚奇，也讓實驗室更有趣了，還有黃棕儂，雖然你比較少來實驗室，但也很謝謝你在我還沒進實驗室前對我的照顧，另外還有黎延垠你竟然拋棄我們提前畢業去了，剛進實驗室時什麼都不懂，多虧你在，告訴與提醒我要做什麼，以及問你光電系的八卦，ㄎ

III

ㄅ，謝謝你們，雖然跟你們只相處了一年，但碩一的那一年裡，因為有你們讓我覺得實驗室很溫馨也讓我能更快熟悉實驗室，當然也要謝謝和我當了兩年同學的李柏毅，謝謝你對我生活上的關心。還有許家瑋，謝謝你很熱心想教我程式語言但我還是沒學會＝＝ 另外，還有實驗室的學弟們，雖然跟你們還沒有很熟，不過也祝你們在實驗室的生活都能很愉快。

　　最後當然要謝謝一位特別的人，謝謝你的陪伴與鼓勵，讓我在心情不好沮喪的時候得以抒發與得到安慰，未來還有很多挑戰等著我們，我們要一起加油！！

　　　　　　　　　　　　　　　　　　　　小布丁 于 九十九年六月

# Contents

# List of Figures

# List of Tables

# Chapter 1 Introduction

## 1.1 Basic property of ZnO and significance of ZnO related photonic devices

Zinc oxide (ZnO) is a promising material for a variety of practical applications [1] such as piezoelectric transducers, optical waveguides, surface acoustic wave devices, varistors, phosphors, solar cells, chemical and gas sensors, transparent electrodes, spin functional devices, UV-light emitters [2] and ultraviolet laser diodes. The basic properties of ZnO can be obtained by examining Table 1-1, which compares the material properties of other relevant semiconductors [3].

| Material | Crystal structure | Lattice constants | | Band gap energy at RT | Cohesive energy | Melting point | Exciton binding energy | Dielectric constants | |
|---|---|---|---|---|---|---|---|---|---|
| | | $a$ (Å) | $c$ (Å) | $E_g$ (eV) | $E_{coh}$ (eV) | $T_m$ (K) | $E_b$ (meV) | $\varepsilon(0)$ | $\varepsilon(\infty)$ |
| ZnO | Wurtzie | 3.249 | 5.207 | 3.37 | 1.89 | 2248 | 60 | 8.75 | 3.75 |
| ZnS | Wurtzie | 3.823 | 6.261 | 3.8 | 1.59 | 2103 | 39 | 9.6 | 5.7 |
| ZnSe | Zinc blende | 5.668 | ⋯ | 2.70 | 1.29 | 1793 | 20 | 9.1 | 6.3 |
| GaN | Wurtzie | 3.189 | 5.185 | 3.39 | 2.24 | 1973 | 21 | 8.9 | 5.35 |
| 6$H$-SiC | Wurtzie | 3.081 | 15.117 | 2.86(ind.) | 3.17 | >2100 | ⋯ | 9.66 | 6.52 |

Table 1-1. Comparison of properties of ZnO with those of other wide band gap semiconductors [3].

ZnO has attracted significant scientific and technological attention due to its wide direct band gap (3.37 eV) that is suitable for photonic applications in the ultraviolet (UV) or blue spectrum range [4]. In this regard, a large exciton binding energy of ZnO is 60 meV, which is significantly larger than that of GaN (25 meV) and

ZnS (39 meV) and other wide-gap semiconductors.  The large exciton binding energy allows stable existence of excitons and efficient excitonic emission at room temperature (thermal energy 26 meV).  The basic material parameters of ZnO are also shown in Table 1-2.  To realize any type of device technology, these parameters are important to have control over the concentration of intentionally introduced impurities (dopants), which are responsible for the electrical properties of ZnO.  The dopants determine whether the current (and, ultimately, the information processed by the device) is carried by electrons or holes.

| Property | Value |
|---|---|
| Lattice parameters at 300 K: $a_0$ $c_0$ $a_0/c_0$ u | 0.32495 nm 0.52069 nm 1.602 (1.633 for ideal hexagonal structure) 0.345 |
| Density | 5.606 g/cm$^3$ |
| Stable phase at 300 K | wurtzite |
| Melting point | 1975°C |
| Thermal conductivity | 0.6, 1-1.2 |
| Linear expansion coefficient (/°C) | $a_0$: 6.5 x 10$^{-6}$, $c_0$: 3.0 x 10$^{-6}$ |
| Static dielectric constant | 8.656 |
| Refractive index | 2.008, 2.029 |
| Energy gap | 3.4 eV (direct) |
| Intrinsic carrier concentration | <10$^6$ /cm$^3$ |
| Exciton binding energy | 60 meV |
| Electron effective mass | 0.24 |
| Electron Hall mobility at 300 K for low *n*-type conductivity | 200 cm$^2$/V·s |
| Hole effective mass | 0.59 |
| Hole Hall mobility at 300 K for low *p*-type conductivity | 5-50 cm$^2$/V·s |

Table 1-2. Properties of wurtzite ZnO.

The structure of ZnO crystal is shown in Fig 1-1 which has a hexagonal wurtzite structure (space group C6mc) with lattice parameters $a$ = 0.3249 nm and $c$ = 0.5207 nm. The structure of ZnO can be simply described as a number of alternating planes composed of tetrahedrally coordinated $O^{2-}$ and $Zn^{2+}$ ions, stacked alternately along the c-axis, in which $a_1$, $a_2$, and c are the unit vectors in a unit cell, the large and small circles denote the anion and cation atoms, respectively. The tetrahedral coordination in ZnO results in non-central symmetric structure and consequently the development of piezoelectricity and pyroelectricity.
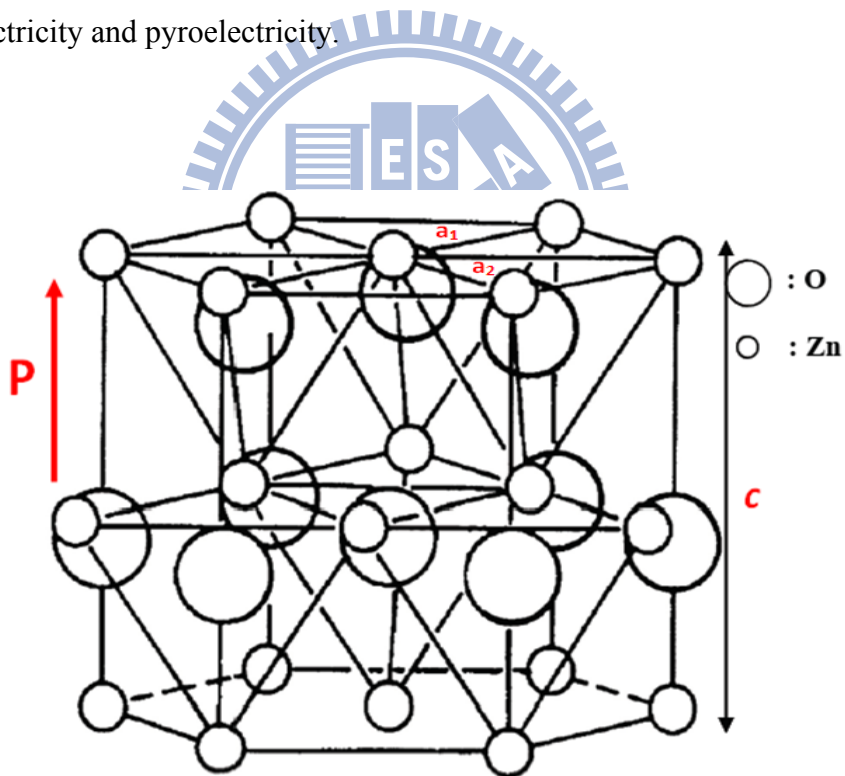


Fig. 1-1 The wurtzite structure model of ZnO.

3

## 1.2 General review of ZnO nanostructures

ZnO nanocrystals have recently attracted broad attention in fundamental studies and technical applications [5] because of their distinguished performance in electronics, optics and photonics. Therefore, in the last few decades, a variety of ZnO nanostructure morphologies, such as nanowires [6], nanorods [7, 8], tetrapods [9], nanoribbons/belts [9], and nanoparticles [10, 11] have been reported. Recently, novel morphologies such as hierarchical nanostructures [12], bridge-/nail-like nanostructures [13], tubular nanostructures [14], nanosheets [15], nanopropeller arrays [16], nanohelixes [17], and nanorings [17] have, amongst others, been demonstrated. These diverse ZnO nanostructures have been fabricated by various methods, such as thermal evaporation [9], metal–organic vapor phase epitaxy (MOVPE) [8], laser ablation, hydrothermal synthesis [7], sol-gel method [10, 11] and template-based synthesis [6]. Several recent review articles have summarized progress in the growth and applications of ZnO nanostructures [4, 18]. Some of the possible ZnO nanostructure morphologies are shown in Fig. 1.2.

Additionally, when the dimension of semiconductors are reduced from three (bulk material) to the quasi-zero dimensional semiconductor structures such as quantum dots (QDs), the optical properties of QDs are much different from the bulk materials. There are two physical mechanisms in modifying the energy band

structure of nanostructures, i.e., the quantum confinement effect (QCE) [19] and surface states [20]. These two mechanisms compete with each other to influence PL spectra. For nanodots or nanostructures in ZnO system with diameters less than 10 nm, the QCE plays a dominant role as has been much reported [21]. On the other hand, the surface-to-volume ratio also brings much influence on the system's Hamiltonian when the material size is reduced to the nanometer scale [22]. The predominance of surface states is responsible for many novel physical features of nanomaterials. In the past decade, various groups have devoted to produce ZnO QDs and study the properties. For instance, Guo et al. [23] exhibited significantly enhanced UV luminescence, diminished visible luminescence and excellent third-order nonlinear optical response with poly vinyl pyrrolidone (PVP) modified surface of ZnO nanoparticles. Pan *et al.* [24] predicted a significant increase in the intensity ratio of the deep level to the near band edge emission is observed with ever-increasing nanorod surface-aspect ratio. Fonoberov et al. [25] have theoretically investigated that, depending on the fabrication technique and ZnO QD surface quality, the origin of UV photoluminescence (PL) in ZnO QDs is either recombination of confined exciton or surface-bound ionized acceptor-exciton complexs. Although there were many experiments to describe the behavior of ZnO nanostructure, more and more unique behaviors are still continuously being explored.
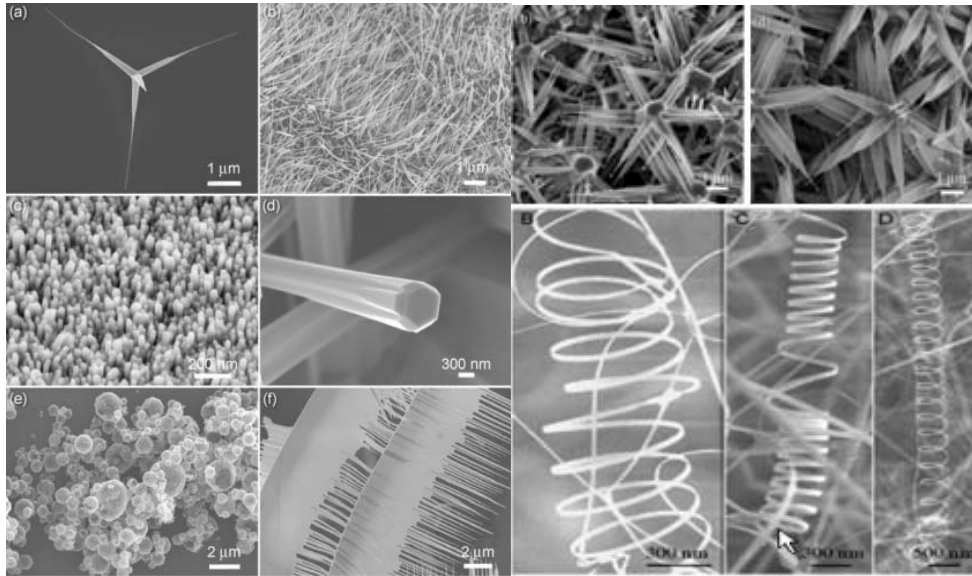
Fig. 1.2 Representative scanning electron microscopy images of various ZnO nanostructure morphologies [4].

## 1.3 Motivations

Recently, the power-dependent photoluminescence (PL) of ZnO bulk associated with biexciton recombination has been investigated by several research groups [26-29]. Zhang et al. [26], who grew ZnO rods by metalorganic chemical vapor deposition, indicated that the biexciton intensity is proportional to the 1.7th power of the excitation density. Besides, we have observed the intensity of biexciton emission in ZnO powder is proportional to the 1.86th power of the excitation power at T = 80 K, but it is close to unity exponent or even sub-linear when it is measured at the lower temperature [30]. Acoustic and optical phonon scatterings playing key roles in efficient exciton relaxation are responsible for bounding two cooled excitons to form

6

biexciton at various temperatures. At low temperature the acoustic phonon scattering is the dominant mechanism for exciton thermalization while the optical phonon scattering will participate in when the exciton kinetic energy approaches to the energy of the lowest optical phonon about T = 80 K. The efficient cooling of exciton with the assistance of optical phonon scattering allows effectively bounding exciton pairs to form biexcitons.

However, Kim et al. [31] have reported the spectra of power-dependent PL in ZnO nanorods synthesized by standard Schlenk techniques remain nearly unchanged spectral profile as increasing the excitation intensity as compared with 40 meV red shift for bulk crystal with their maximum excitation intensity. They attributed this finding to the quantum confinement effects that can alter the properties of exciton states and claimed in this study the exciton states of the nanorods are stable even when the excitation intensity reaches the Mott density of the bulk crystal due to a smaller exciton size and an enhanced exciton binding energy [32]. On the other hand, Bagnall et al. [33] have observed the red-shifted PL peak of ~50 meV in ZnO powder that may be attributed to the exciton-exciton scattering (or P band) rather than electron-hole plasma (EHP or N band) with > 100 meV red shift.

The characterizations of ZnO QDs are complicated problems to be investigated. And, it is imperative to understand the optical properties of ZnO QDs since they play

important roles in stimulated emission and gain process in real photonic device structures.

## 1.4 Organization of the thesis

This thesis is organized as follows. Chapter 2 covers the theoretical background of experiments such as sol-gel method, X-ray diffraction (XRD), photoluminescence (PL) characterization, and a general concept of quantum effect, fundamental optical transitions and ZnO excitons-related emissions. In Chapter 3, we describe the experimental details including the measurement apparatus and processes. By means of the XRD and PL spectroscopy, the crystal structures and the optical emission properties of ZnO QDs grown by the sol-gel method will be investigated and discussed in Chapter 4. Finally, in Chapter 5, we conclude the studies on the ZnO QDs and propose several topics of the future works.

# Chapter 2 Theoretical background

## 2.1 Sol-gel method

An aerosol is a colloidal suspension of particles in a gas (the suspension may be called a fog if the particles are liquid and a smoke if they are solid) and an emulsion is a suspension of liquid droplets in anther liquid.   A sol is a colloidal suspension of solid particles in a liquid, in which the dispersed phase is so small (~1-1000 nm) that gravitational force is negligible and interactions are dominated by the short-range forces, such as Van der Waals attraction and surface charge.   All of these types of colloids can be used to generate polymers or particles from which ceramic materials can be made.   A polymer is a huge molecule (also called a macromolecule) formed from hundreds or thousands of units called monomers.   If one molecule reaches macroscopic dimensions so that it extends throughout the solution, the substance is said to be gel.

Sol-gel synthesis has two ways to prepare solution.   One way is the metal-organic route with metal alkoxides in organic solvent; the other way is the inorganic route with metal salts in aqueous solution.   It is much cheaper and easier to handle than metal alkoxides, but their reactions are more difficult to control.   The inorganic route is a step of polymerization reactions through hydrolysis and

condensation of metal alkoxides M(OR)$_Z$, where M = Si, Ti, Zr, Al, Sn, Ce, and OR is

an alkoxy group and Z is the valence or the oxidation state of the metal.  First,

hydroxylation upon the hydrolysis of alkoxy groups:

$$M - OR + H_2O \rightarrow M - OH + ROH \ .$$
(2-1)
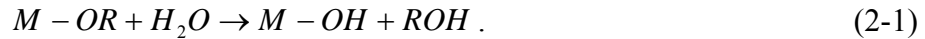
The second step, polycondensation process leads to the formation of branched

oligomers and polymers with a metal oxygenation based skeleton and reactive

residual hydroxyl and alkoxy groups.  There are 2 competitive mechanisms:

(1) Oxolation-- formation of oxygen bridges:

$$M - OH + XO - M \rightarrow M - O - M + XOH \ .$$
(2-2)
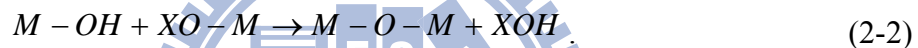
The hydrolysis ratio (h = H$_2$O/M) decides X=H (h >> 2) or X = R (h < 2).

(2) Olation-- formation of hydroxyl bridges when the coordination of the metallic

center is not fully satisfied (N - Z > 0):

$$M - OH + HO - M \rightarrow M - (OH)_2 - M \ ,$$
(2-3)
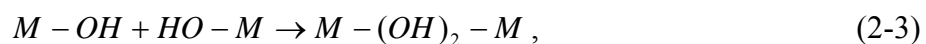
where X = H or R.  The kinetics of olation is usually faster than those of oxolation.

Figure 2-1 presents a schematic of the routes that one could follow within the

scope of sol-gel processing [34].  In the sol-gel process, the precursors (starting

compounds) for preparation of a colloid consist of a metal or metalloid element

surrounded by various ligands.  The precursors were mixed together and heated at

high temperature.  This procedure has to be repeated several times until a

homogeneous product is obtained.   Then, the materials have to be transformed into

the desired shape.   For example, an alkyl is a ligand formed by removing one

hydrogen (proton) from an alkane molecule to produce, for example, methyl ($\cdot CH_3$)

or ethyl ($\cdot C_2H_5$).   An alcohol is a molecule formed by adding a hydroxyl (OH) group

to an alkyl (or other) molecule, as in methanol ($CH_3OH$) or ethanol ($C_2H_5OH$).

Metal alkoxides are members of the family of metalorganic compounds, which

have an organic ligand attracted to a metal or metalloid atom.   Metal alkoxides are

popular precursors because they react readily with water.   The reaction is called

hydrolysis, because a hydroxy ion becomes attached to the metal atom.   This type of

reaction can continue to build larger and larger molecules by the process of

polymerization.   The gel point is the time (or degree of reaction) when the last bound

is formed that completes this giant molecule.   It is generally found that the process

begins with the formation of fractal aggregates that begin to impinge on one another,

then those clusters link together as described by the theory of percolation.   The gel

point corresponds to the percolation threshold, when a single cluster (call the

spanning cluster) appears that extends throughout the sol; the spanning cluster

coexists with a sol phase containing many smaller clusters, which gradually become

attached to the network.   Gelation can occur after a sol is cast into a mold, in which

it is possible to make objects of a desired shape.

**Overview of the sol-gel process**
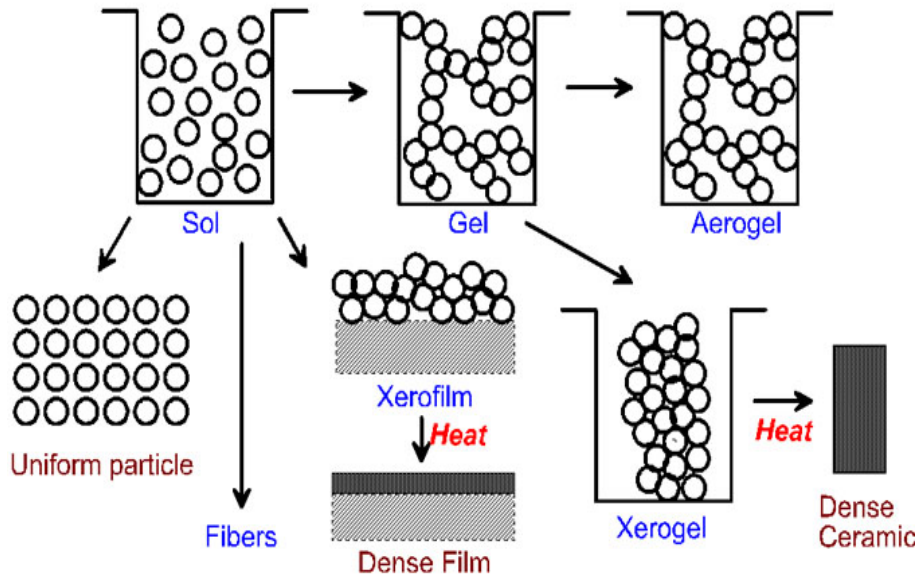
Fig. 2-1 Schematic of the rotes that one could follow within the scope of sol-gel processing [8].

## 2.2 Quantum effect

During the last decade, the growth of low-dimensional semiconductor structures has made it possible to reduce the dimension from three (bulk material) to the quasi-zero dimensional semiconductor structures usually called QDs. In these nanostructures the quantum confinement effects become predominant and give rise to many interesting electronic and optical properties. The electron energy will be quantized and varies with dot sizes that cause the variation of band gap energy, binding energy, and Bohr radius. The band gap and the density of states (DOS) associated with a quantum-structure differ from that associated with bulk material, determined from the magnitude of the three-dimension wave vector.

12

**2.2.1 Quantum confinement effect**

Models explaining the confinement of charged particles in a three-dimensional potential well typically involve the solution of Schrödinger's wave equation using the Hamiltonian [35]

$$H = -\frac{\hbar^2}{2m_e}\nabla^2 - \frac{\hbar^2}{2m_h}\nabla^2 + V_0 + U \ . \tag{2-4}$$

Variation between treatments generally originates from differences in expressions assigned to $V_0$ for the confining potential well, which normally is accompanied by the Coulombic interaction term U. Boundary conditions are imposed forcing the wave functions describing the carriers to zero at the walls of the potential well.

Two regimes of quantization are usually distinguished in which the crystallite radius R is compared with the Bohr radius of the excitons $a_B$ or the related quantities:

(1) Weak confinement regime for $R \geq a_B$ and

(2) Strong confinement regime for $R < a_B$ .

In the weak confinement regime, the motion of center of exciton mass is quantized while the relative motion of electron and hole given by the envelope function $\phi(r_e - r_h)$ is hardly affected. In the strong confinement regime, however, the Coulomb energy increases roughly with $R^{-1}$, and the quantization energy with $R^{-2}$, so that for sufficiently small values of R one should reach a situation where the

Coulomb term can be neglected.

2.2.1.1 Weak confinement [36]

Coulomb-related correlation between the charged particles handled through the use of variational approach involving higher-order wave function of the confined particles, and we cannot neglect the electron hole Coulomb potential. The Schrödinger equation may be written as

$$(-\frac{\hbar^2}{2m_e} - \frac{\hbar^2}{2m_h})\nabla^2\Psi + [V_0 + U(r_e - r_h)]\Psi = E_t\Psi .$$
(2-5)

Taking $r = r_e - r_h$ and $R = \frac{m_e r_e + m_h r_h}{m_e + m_h}$, then the equation becomes

$$[-\frac{\hbar^2}{2M}\nabla_R^2 - \frac{\hbar 2}{2\mu}\nabla_r^2 + V(R) + U(r)]\Psi = E_t\Psi$$

with $M = m_e + m_h$, $\mu = \frac{m_e m_h}{m_e + m_h}$, and $E_t$ as the total energy of the system. If we take $\Psi = \phi(R)\varphi(r)$ and consider Coulomb interaction first, then we get

$$[-\frac{\hbar^2}{2M}\nabla_R^2 + V(R)]\phi(R) = E_c\phi(R) ,$$

$$[-\frac{\hbar^2}{2\mu}\nabla_r^2 + U(r)]\varphi(r) = (E_t - E_c)\varphi(r) = E_{ex}\varphi(r) .$$

Here $E_{ex}$ results from the inclusion of Coulomb interaction. Then we consider the confinement potential

$$V(R) = 0, R \le a_B$$
$$V(R) = \infty, R > a_B$$
.

Thus, the energy is

$$E_{cn} = \frac{\hbar^2\pi^2 n^2}{2Ma^2}, n = 1,2,3.....$$
(2-6)

and the absorption energy of a photon is

$$\hbar\omega_0 = E_t = E_c + E_{ex} = E_g + \frac{\hbar^2\pi^2}{2Ma^2} + E_{ex} \qquad (2\text{-}7)$$

with $M = m_e + m_h$ as the total mass of the electron and hole.

2.2.1.2 Strong confinement

The size quantization band states of the electron and hole dominate for the kinetic energies of electron and hole are larger than the electron-hole Coulomb potential, and the effect of the Coulomb attraction between the electron and hole can be treated as a perturbation.　Then the Schrödinger equation becomes

$$(-\frac{\hbar^2}{2m_e} - \frac{\hbar^2}{2m_e})\nabla^2\Psi + V_0\Psi = E\Psi .$$

The potential is defined as

$$V(r) = 0, r \le a_B$$
$$V(r) = \infty, r > a_B$$

and the energy of an electron or a hole is

$$E_{cn} = \frac{\hbar^2\pi^2 n^2}{2m_{e,h}a^2}, n = 1,2,3.....$$

The absorption energy of a photon is

$$\hbar\omega_0 = E_g + \frac{\hbar^2\pi^2}{2a^2}(\frac{1}{m_e} + \frac{1}{m_h}) = E_g + \frac{\hbar^2\pi^2}{2a^2\mu} \qquad (2\text{-}8)$$

with $\mu = \dfrac{m_e m_h}{m_e + m_h}$ as the reduced mass of electron and hole.

**2.2.2 Density of states (DOS)**

The concept of density of states (DOS) is extremely powerful and important physical properties such as optical absorption, transport, etc., are intimately dependent upon this concept. The density of states is the number of available electronic states per unit volume per unit energy around an energy $E$. If we denote the density of states by $N(E)$, the number of states in an energy interval $dE$ around an energy $E$ is $N(E)dE$. To calculate the density of states, we need to know the dimensionality of the system and the energy vs. wave vector relation or the dispersion relation that the electrons obey [37].

**2.2.2.1 Density of states for a three-dimensional system**

In a three dimension system, the k-space volume between vector $k$ and $k + dk$ is $4\pi k^2 dk$ (see Figure 2-2). We had shown above that the $k$-space volume per electron state is $(2\pi / L)^3$. Therefore, the number of states of electron in the region between $k$ and $k + dk$ are

$$\frac{4\pi k^2 dk}{8\pi^3} V = \frac{k^2 dk}{2\pi^2} V .$$

Denoting the energy and energy interval corresponding to $k$ and $dk$ as $E$ and $dE$, we see that the number of electron states between $E$ and $E + dE$ per unit volume are

$$N(E)dE = \frac{k^2 dk}{2\pi^2}$$

and since $E = \dfrac{\hbar^2 k^2}{2m}$, then the equation becomes

$$k^2 dk = \frac{\sqrt{2} m^{\frac{3}{2}} E^{\frac{1}{2}} dE}{\hbar^3},$$

which gives

$$N(E)dE = \frac{m^{\frac{3}{2}} E^{\frac{1}{2}}}{\sqrt{2}\pi^2 \hbar^3} dE.$$

We must remember that the electron can have two states for a given $k$-value

since it can have a spin state of $s = 1/2$ or $-1/2$.   Accounting for spin, the density of

states is

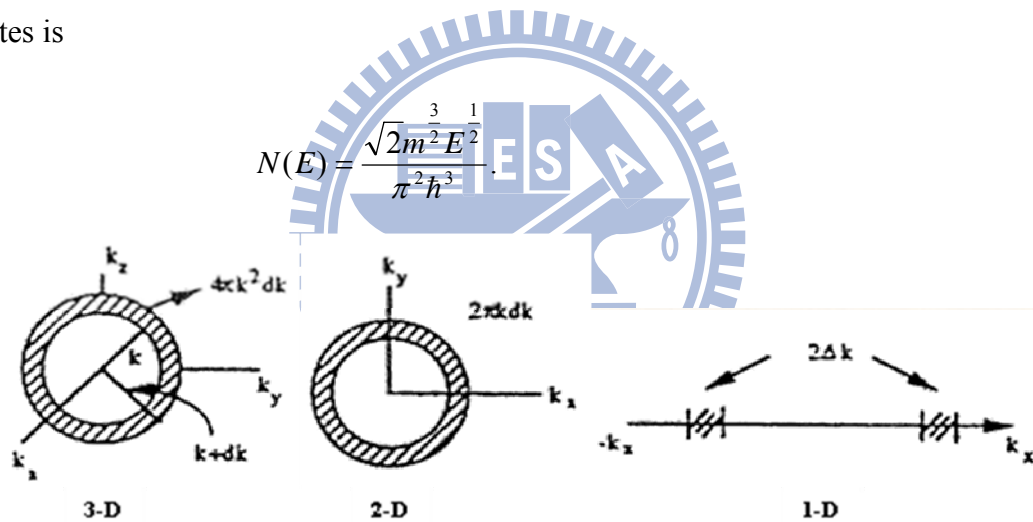$$N(E) = \frac{\sqrt{2} m^{\frac{3}{2}} E^{\frac{1}{2}}}{\pi^2 \hbar^3}.$$



Fig. 2-2 Geometry used to calculate density of states in three, two and one dimensions.

## 2.2.2.2 Density of states for lower-dimensional systems

If we consider a 2-D system, a concept that has become a reality with use of

quantum wells, similar arguments tell us that the density of states for a parabolic band

is

$$N(E) = \frac{m}{\pi\hbar^2}.$$

Finally, in a 1-D system or "quantum wire", the density of states is

$$N(E) = \frac{\sqrt{2}m^{\frac{1}{2}}E^{-\frac{1}{2}}}{\pi\hbar}.$$

We notice that as the dimensionality of the system changes, the energy dependence of the density of states also changes. In three-dimensional systems we have $E^{1/2}$-dependence as shown in Figure 2-3a, while in two-dimensional systems there is no energy dependence (Figure 2-3b). In one-dimensional systems, the density of states has $E^{-1/2}$-dependence and a peak at $E = 0$ (Figure 2-3c), and the density of states in zero-dimensional systems is shown in Figure 2-3d. The variations related to dimensionality are extremely important and is a key driving force to lower dimensional systems.
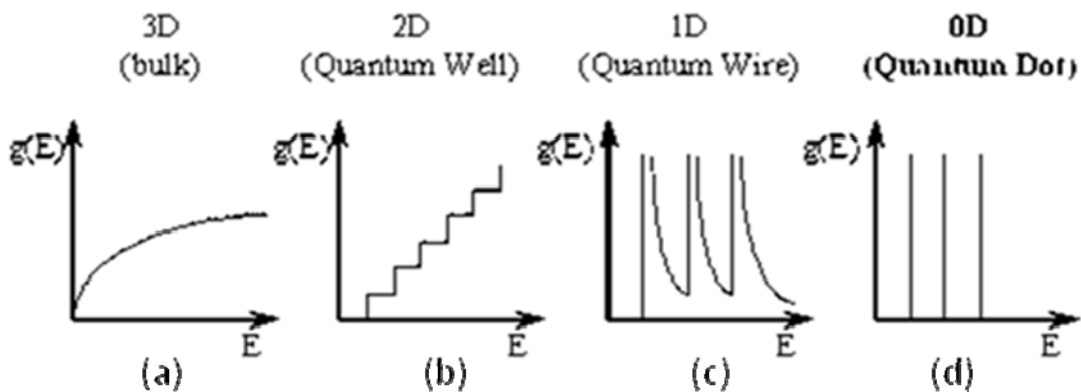


Fig. 2-3 Variation in the energy dependence of the density of states in a) three-dimensional b) two-dimensional c) one-dimensional d) zero-dimensional systems.

## 2.3 X-ray diffraction

### 2.3.1 Lattice parameters [38]

A crystal consists of orderly array of atoms, each of which can scatter electromagnetic waves. A monochromatic beam of X-rays that falls upon a crystal will be scattered in all directions inside it. However, owing to the regular arrangement of the atoms, in certain directions the scattered waves will constructively interfere with one another while in others they will destructively interfere. The peaks of an x-ray diffraction pattern are made up of photons constructively interfere with planes, this analysis was suggested in 1913 by W. L. Bragg. Consider an incident monochromatic x-ray beam interacting with the atoms arranged in a periodic manner as shown in 2-dimendion in Fig. 2-4. The atoms represented as circles in the graph form different sets of plane in the crystal. To give a set of lattice planes with an inter-plane distance of d, the condition for diffraction (peak) constructively interfere to occur can be simply written as

$$2d \sin \theta = n\lambda , \qquad n = 1,2,3,... , \qquad (2.9)$$

which is known as the Bragg's law. In this equation, $\lambda$ is the wavelength of the x-ray, $\theta$ is the diffraction angle, and n is an integer representing the order of the diffraction peak.
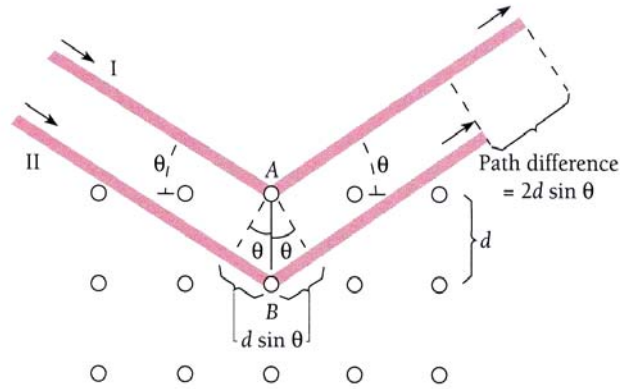
Fig. 2-4 x-ray scattering from a 2-dimendion periodic crystal.

The lattice constant can be found by means of the diffraction pattern. For hexagonal unit cell (Figure 2-5), which is characterized by lattice parameters a and c, the plane spacing equation for hexagonal structure is

$$\frac{1}{d^2} = \frac{4}{3}\left(\frac{h^2 + hk + k^2}{a^2}\right) + \frac{l^2}{c^2},$$

(2.10)

where $h$, $k$, and $l$ are the Mill's indices.

Combining the Bragg's law ($\lambda = 2d\sin\theta$) with (2-2), we can get:

$$\frac{1}{d^2} = \frac{4}{3}\left(\frac{h^2 + hk + k^2}{a^2}\right) + \frac{l^2}{c^2} = \frac{4\sin^2\theta}{\lambda^2}.$$

(2-11)

Rearranging (2-3) gives

$$\sin^2\theta = \frac{\lambda^2}{4}\{\frac{4}{3}\left(\frac{h^2 + hk + k^2}{a^2}\right) + \frac{l^2}{c^2}\},$$

(2-12)

thus the lattice parameters can be estimated from Eq. (2-12).
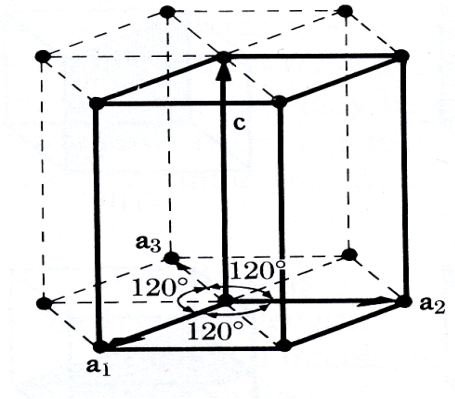
Fig. 2-5 The hexagonal unit cell.

## 2.3.2 Deby-Scherer formula [39]

Considering the path difference between the successive planes when the incident beam remains fixed at the Bragg angle θ, but with the diffracted ray leaving at an angle θ+Δθ, corresponding to intensity $I$ in the spectrum line an distance Δθ away from the peak as Figure 2-6.
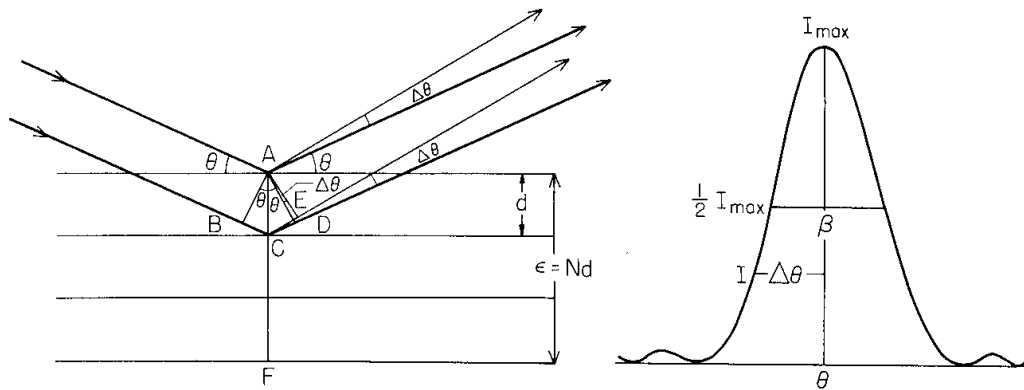


Fig. 2-6 Grating treatment of line broadening by crystallite.

The path difference between waves from successive planes is now

$$BC + CE = d\sin\theta + d\sin(\theta+\Delta\theta)$$

$$= d\sin\theta + d\sin\theta\cos\Delta\theta + d\cos\theta\sin\Delta\theta \qquad (2.13)$$

where BC and CE is the path difference between incident ray of the successive planes, and d is the interplanar distance. If $\Delta\theta$ is very small, we can write $\cos\Delta\theta\approx 1$ and $\sin\Delta\theta\approx\Delta\theta$, in which case

$$BC + CE = 2d\sin\theta + d\cos\theta\Delta\theta. \qquad (2.14)$$

Combining Bragg's law Eq. (2.1)

$$BC + CE = 2d\sin\theta + d\cos\theta\Delta\theta = n\lambda + d\cos\theta\Delta\theta, \qquad (2.15)$$

where $\lambda$ is the wavelength of the incident x-ray. Therefore the phase difference $\delta$ per interplanar distance or "aperture" is

$$\delta = n\lambda\frac{2\pi}{\lambda} + \frac{2\pi}{\lambda}d\cos\theta\bullet\Delta\theta$$
$$= 2n\pi + \frac{2\pi}{\lambda}d\cos\theta\bullet\Delta\theta \qquad (2.16)$$

Since a phase difference of $2\pi n$ produces the same effect as a zero phase, we can write the effective phase difference per aperture as

$$\delta = \frac{2\pi}{\lambda}d\cos\theta\bullet\Delta\theta \qquad (2.17)$$

We obtain the result that the distribution of intensity of $I$ in a spectrum line a distance R from the grating is effectively

$$I = (\frac{\Phi}{R})^2\frac{\sin^2\frac{1}{2}N\delta}{\sin^2\frac{1}{2}\delta} \qquad (2.18)$$

and maximum intensity is

$$I_{max} = (\frac{\Phi}{R})^2 N^2 . \tag{2.19}$$

where $\Phi$ is the amplitude at unit distance from the graying, and N is the total number

of grating aperture.

Diving Eq. (2.10) by Eq. (2.11), we obtain

$$\frac{I}{I_{max}} = \frac{\sin^2 \frac{1}{2} N\delta}{\sin^2 \frac{1}{2} \delta} (\frac{1}{N})^2 . \tag{2.20}$$

Since $\frac{1}{2} N\delta$ will change much faster than $\frac{1}{2} \delta$, the function will reach its first

minimum before $\frac{1}{2} \delta$ is very large. We can therefore replace $\sin \frac{1}{2} \delta$ by $\frac{1}{2} \delta$, and

we will get

$$\frac{I}{I_{max}} = (\frac{\sin \frac{1}{2} N\delta}{\frac{1}{2} N\delta})^2 . \tag{2.21}$$

The ratio $\frac{I}{I_{max}}$ will fall to $\frac{1}{2}$ when

$$\frac{\sin \frac{1}{2} N\delta}{\frac{1}{2} N\delta} = \frac{1}{\sqrt{2}} . \tag{2.22}$$

The solution to the equation (2.14) yields the required phase difference

corresponding to the half maximum. It may be obtained

$$\frac{1}{2} N\delta = 1.39, \tag{2.23}$$

Since, according to equation (2.9), $\delta = \frac{2\pi}{\lambda} d \cos\theta \bullet \Delta\theta$ , and D = Nd, we obtain

$$\frac{0.89\lambda}{D\cos\theta} = 2\Delta\theta . \tag{2.24}$$

23

Let B be taken as the full width at half maximum from $\Delta\theta$ to $-\Delta\theta$, hence

$$B = 2\Delta\theta = \frac{0.89\lambda}{D\cos\theta} \quad \text{(radians)}, \tag{2.25}$$

where $\lambda$ is the wavelength of x-ray and D is the average size of the particles.

## 2.4 Photoluminescence characterization [35, 40]

Photoluminescence (PL) is a powerful and noninvasive optical analysis technology for the semiconductor industry. It has high sensitivity to reveal the band structure and the carrier transportation behaviors in a material. From PL spectrum the defect or impurity can also be found in the compound semiconductors, which affect material quality and device performance. A given impurity produces a set of characteristic spectral features. The fingerprint identifies the impurity type, and often several different impurities can be seen in a single PL spectrum. In addition, the full width at half maximum of the PL peak is an indication of sample's quality [41]. So the PL could be a judgment of the material quality and be a key technology of the development of nano-technology.

PL is the optical radiation emitted by a physical system (in excess the thermal equilibrium blackbody radiation) resulting from excitation to a nonequilibrium state by illuminating with light. Three processes can be distinguished: (i) creation of electron-hole pairs by absorption of the excited light, (ii) radiative recombination of

electron-hole pairs, and (iii) escape of the recombination radiation from the sample.

### 2.4.1 Fundamental Transitions

An electron is excited from the valence band to the conduction band by absorption of a photon. In this sense an optical excitation is a two-particle transition. The same is true for the recombination process. An electron in the conduction band can return radiatively or nonradiatively to the valance band only if there is a free space, i.e., a hole available. Two quasi-particles annihilate in the recombination process. What we need for the understanding of the optical properties of the electronic system of a semiconductor is therefore a description of the excited states of the N-particle problem. We will consider the fundamental transitions, those occurring at or near the band edges.

1.   Free excitons (Wannier-Mott excitons)

An electron in the conduction band and a hole in the valence band are created at the same point in space and can attract each other through their Coulomb interaction. Using the effective mass approximation, the Coulomb interaction between electron and hole leads to a hydrogen-like problem with a Coulomb potential term

$$\frac{-e^2}{4\pi\varepsilon_0\varepsilon\left|r_e - r_h\right|}.$$

Here we will consider the so-called Wannier-Mott excitons more specifically. This type of excitons has a large Bohr radius (i.e., the mean distance between electron and hole) that encompasses many atoms, and they are delocalized states that can move freely throughout the crystal; hence the alternative name of free excitons.

Indeed excitons in semiconductors form, to a good approximation, a hydrogen- or positronium-like series of states below the gap. For a simple parabolic band in a direct-gap semiconductor one can separate the relative motion of electron and hole and the motion of the center of mass. This leads to the dispersion relation of exciton as shown in Fig. 2-7.

$$E_{ph}(n_B, K) = E_g - Ry^* \frac{1}{n_B^2} + \frac{\hbar^2 K^2}{2M}, \qquad (2.26)$$

where $n_B = 1,2,3,...$ is the principal number, $Ry^* = 13.6(\frac{\mu}{m_0} \frac{1}{\varepsilon^2})$ eV is exciton binding energy, $M = m_e + m_h$ and $K = k_e + k_h$ are translational mass and wave vector of the exciton, respectively. The series of exciton states in (2.26) has an effective Rydberg energy $Ry^*$ modified by the reduced mass of electron and hole and the dielectric constant of the medium in which these particles move. The radius of the exciton equals the Bohr radius of H atom again modified by $\varepsilon$ and $\mu$. Using the material parameters for typical semiconductors one finds that the orbits of electron and hole around their common center of mass average over many unit cells and this in turn justifies the effective mass approximation in a self-consistent way. These
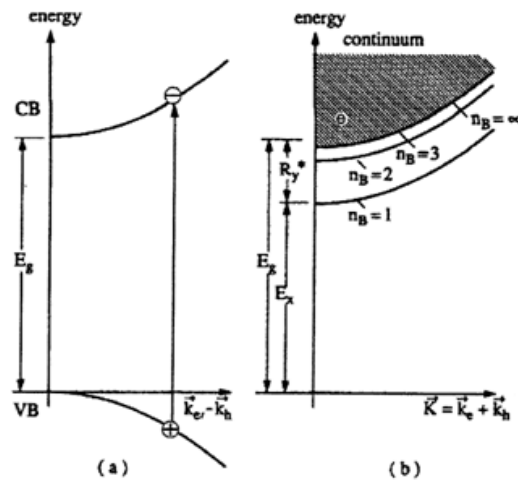
excitons are called Wannier-Mott excitons.



Fig. 2-7 A pair excitation in the scheme of valence and conduction bands (a) in the exciton picture for a direct gap semiconductor (b).

## 2. Biexcitons

It is well known that two hydrogen atoms with opposite electron spins can bind to form a hydrogen molecule. In the same sense, it has been calculated that two positronium-like atoms can form a positronium-like molecule as a bound state. So the idea is not far away that two excitons could bind to form a new quasiparticle, the so-called biexciton or excitonic molecule. It has been found theoretically that the biexciton should form a bound state for all ratios of effective electron and hole masses and dimensionalities of the sample.

The dispersion relation is given in the simplest case by

$$E_{biex}(k) = 2(E_g - E_{ex}^b) - E_{biex}^b + \frac{\hbar^2 k^2}{4M_{ex}}, \tag{2-27}$$

assuming that the effective mass of the biexciton is just twice that of the exciton.

### 3. Bound excitons

Similar to the way that free carriers can be bound to defects, it is found that excitons can also be bound to defects. Some of these defects can bind an exciton resulting in a bound exciton complex (BEC). In Figure 2-8 we visualize exciton bound to an ionized donor ($D^+X$), a neutral donor ($D^0X$), and a netural axxeptor ($A^0X$). An ionized acceptor does not usually bind an exciton since a neutral acceptor and a free electron are energetically more favorable. The binding energy of an exciton (X) is the highest for a neutral acceptor ($A^0X$ complex), the lower for a neutral donor ($D^0X$) and the lower still for an ionized donor ($D^+X$). The binding energy $E^b$ of exciton to the complex usually increases according to $E^b_{D^+X} < E^b_{D^0X} < E^b_{A^0X}$. The binding energy is defined as the energetic distance from the lowest free exciton state at k = 0 to the energy of the complex. There is a rule of thumb, known as Hayne's rule, which relates the binding energy of the exciton to the neutral complex with the binding of the additional carrier to the point defect.
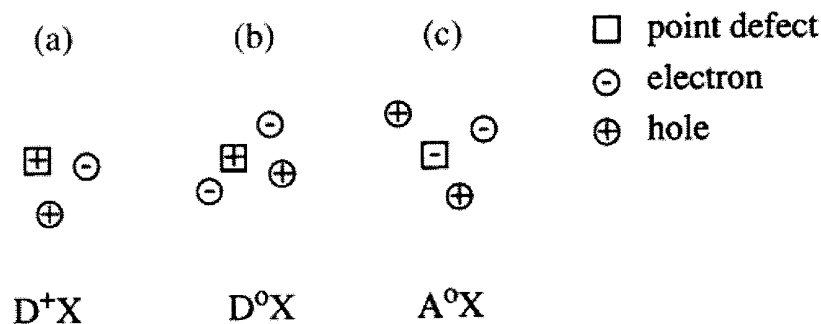


Fig. 2-8 Visualization of an exciton bound to an ionized donor (a), a neutral donor (b), and a neutral acceptor (c).

4. Surface-bound exciton

The surface-to-volume ratio brings much influence on the system's Hamiltonian when the material size is reduced to the nanometer scale [22]. From the calculation of exciton states at the QD surface, we can know the exciton is bound to the surface-located acceptor [25]. Unlike the acceptor, the donor does not bind the exciton. Because the hole is much heavier than the electron, which makes the surface donor a shallow impurity, while the surface acceptor a deep impurity. Therefore, excitons can be effectively bound only to surface acceptors.

5. Two-Electron Satellites (TES) [42]

Two-electron satellite (TES) transitions involve radiative recombination of an exciton bound to a neutral donor, leaving the donor in the excited state. In the effective mass approximation, the energy difference between the ground-state neutral donor bound excitons and their excited states (TES) can be used to determine the donor binding energies [43] (the donor excitation energy from the ground state to the first excited state equals to 3/4 of the donor binding energy, $E_D$) and catalog the different species present in the material.

6.    Donor-Acceptor Pairs (DAP)

Donors and acceptors can form pairs and act as stationary molecules imbedded in the host crystal.    The coulomb interaction between a donor and an acceptor results in a lowering of their binding energies.    In the donor-acceptor pair case it is convenient to consider only the separation between the donor and the acceptor level:

$$E_{pair} = E_g - (E_D + E_A) + \frac{q^2}{\varepsilon r} , \qquad (2-28)$$

where $r$ is the donor-acceptor pair separation, $E_D$ and $E_A$ are the respective ionization energies of the donor and the acceptor as isolated impurities.

7.    Deep transitions

By deep transition we shall mean either the transition of an electron from the conduction band to an acceptor state or a transition from a donor to the valence band in Fig. 2-9.    Such transition emits a photon $h\nu = E_g - E_i$ for direct transition and $h\nu = E_g - E_i - E_p$ if the transition is indirect and involves a phonon of energy $E_p$. Hence the deep transitions can be distinguished as （Ⅰ）conduction-band-to-acceptor transition, which produces an emission peak at $h\nu = E_g - E_A$ , and （Ⅱ） donor-to-valence-band transition which produces emission peak at the higher photon energy $h\nu = E_g - E_D$ .
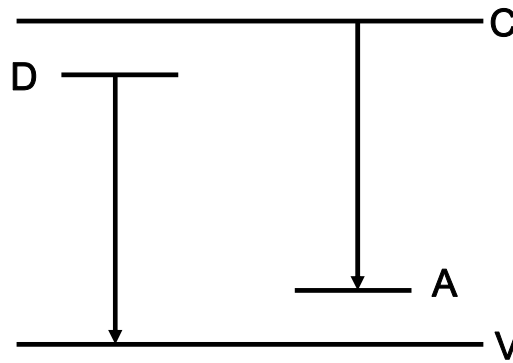
Fig. 2-9 Radiative transition between a band and an impurity state.

## 2.4.2 Influence of high excited light intensity

The PL conditions as mentioned above are excited by low excitation light intensity. At low excitation light intensity (low density regime in Fig. 2-10), the PL properties are determined by single electron-hole pairs, either in the exciton states or in the continuum. Higher excitation intensity (intermediate density regime in Fig. 2-10) makes more excitons; such condition would lead to the exciton inelastic scattering processes and form the biexciton. The scattering processes may lead to a collision-broadening of the exciton resonances and to the appearance of new luminescence bands, to an excitation-induced increase of absorption, to bleaching or to optical amplification, i.e., to gain or negative absorption depending on the excitation conditions. If we pump the sample even harder, we leave the intermediate and arrive at the high density regime in Fig. 2-10, where the excitons lose their identity as individual quasiparticles and where a new collective phase is formed which
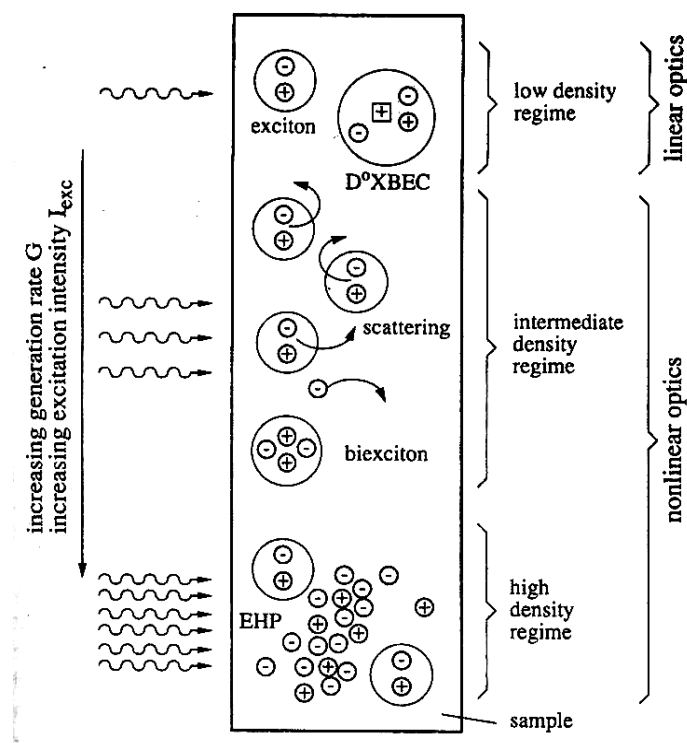
31

is known as the electron-hole plasma (EHP).



Fig. 2-10 The general scenario for many-particle effects in semiconductors. [35]

## 1. Electron-Hole Plasma

In this high density regime, the density of electron-hole pairs $n_p$ is at least in parts of the excited volume so high that their average distance is comparable to or smaller than their Bohr radius, i.e., we reach a "critical density" $n_p^c$ in an EHP, given to a first approximation by $a_B^3 n_p^c \approx 1$. We can no longer say that a certain electron is bound to a certain hole; instead, we have the new collective EHP phase. The transition to an EHP is connected with very strong changes of the electronic excitations and the optical properties of semiconductors.

2. Scattering Processes

In the inelastic scattering processes, an exciton is scattered into a higher excited state, while another is scattered on the photon-like part of the polariton dispersion and leaves the sample with high probability as a luminescence photon, when this photon-like particle hits the surface of the sample. This process is shown schematically in Fig. 2-11 and the photons emit in such a process having energies $E_n$ given by Ref. [44]

$$E_n = E_{ex} - E_b^{ex}\left(1-\frac{1}{n^2}\right) - \frac{3}{2}kT , \qquad (2\text{-}29)$$

where n = 2, 3, 4,…, $E_b^{ex} = 60$ meV is the binding energy of the free exciton of ZnO, and kT is the thermal energy. The resulting emission bands are usually called P-bands with an index given by n.
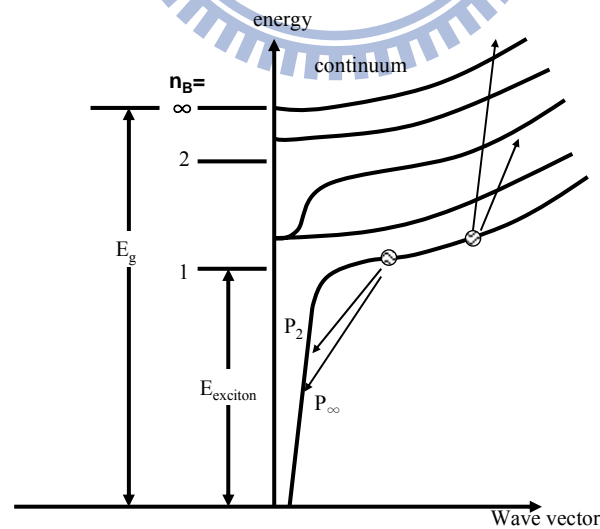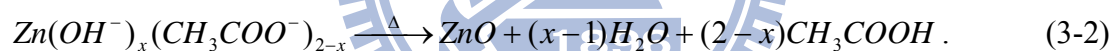


Fig.2-11 Schematic representation of the inelastic exciton-exciton scattering processes [35].

# Chapter 3 Experiment details and analysis techniques

## 3.1 Sample preparation

We fabricate ZnO QDs by sol-gel method.  Sol-gel method was chosen due to its simple handling, low cost, and narrow size distribution.  In particular, it has the potential to produce samples with large areas and complicated forms on various substrates.
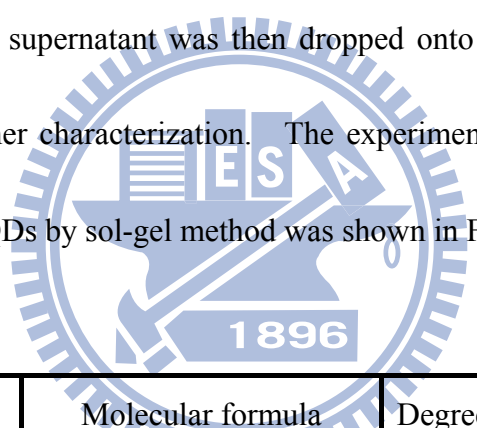
The ZnO colloidal spheres were produced by one-stage reaction process, and reactions were described as the following equations:

$$Zn(CH_3COO)_2 + xH_2O \xrightarrow{\Delta} Zn(OH^-)_x(CH_3COO^-)_{2-x} + xCH_3COOH , \qquad (3\text{-}1)$$

$$Zn(OH^-)_x(CH_3COO^-)_{2-x} \xrightarrow{\Delta} ZnO + (x-1)H_2O + (2-x)CH_3COOH . \qquad (3\text{-}2)$$

Equation (3-1) is the hydrolysis reaction for $Zn(OAc)_2$ to form metal complexes.  We increased the temperature of reflux from RT to 160$^o$C and maintained for aging.  The zinc complexes will dehydrate and remove acetic acid to form pure ZnO as Eq. (3-2) during the aging time.  Actually, the two reactions described above proceed simultaneously while the temperature is over 110$^o$C.

All chemicals used in this study were reagent grade and employed without further purification.  A typical reaction was listed in Table 3-1, stoichiometric zinc acetate dihydrate [99.5% $Zn(OAc)_2 \cdot 2H_2O$, Riedel-deHaen] was dissolved into

diethylene glycol [99.5% DEG, ethylenediamine-tetra-acetic acid (EDTA)] to make

0.1 M, 0.05 M, 0.01 M solutions.    The first thing we notice is that we can control the

QDs size with domination concentration of zinc acetate in the solvent (DEG).    Then

the temperature of reaction solution was increased to $160°C$, and white colloidal ZnO

was formed in the solution that was employed as the primary solution.    The primary

solutions were put separately in a centrifuge operating at 3000 rpm for 30 minutes.

The supernatant was decanted off and saved, and the polydisperse powder was

discarded.    Finally, the supernatant was then dropped onto Si (100) substrates and

dried at $150°C$ for further characterization.    The experiment equipment and a flow

chart of fabricate ZnO QDs by sol-gel method was shown in Figure 3-1&3-2.

| Chemical reagent | Molecular formula | Degree of purity | Source |
|---|---|---|---|
| Zinc acetate dehydrate | $Zn(CH_3COOH)_2 \cdot 2H_2O$ | 99.5% | Riedel-deHaen |
| Diethylene glycol | $C_4H_{10}O_3$ | 99.5% | EDTA |

Table 3-1 Shows that chemical reagent was used with sol-gel experiment process.
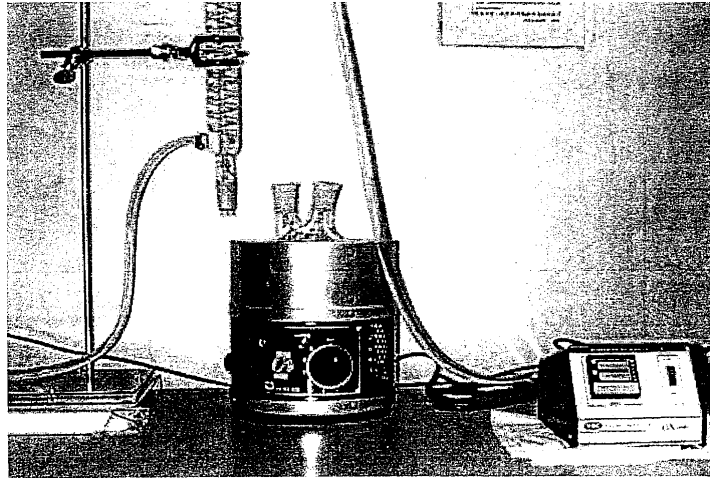
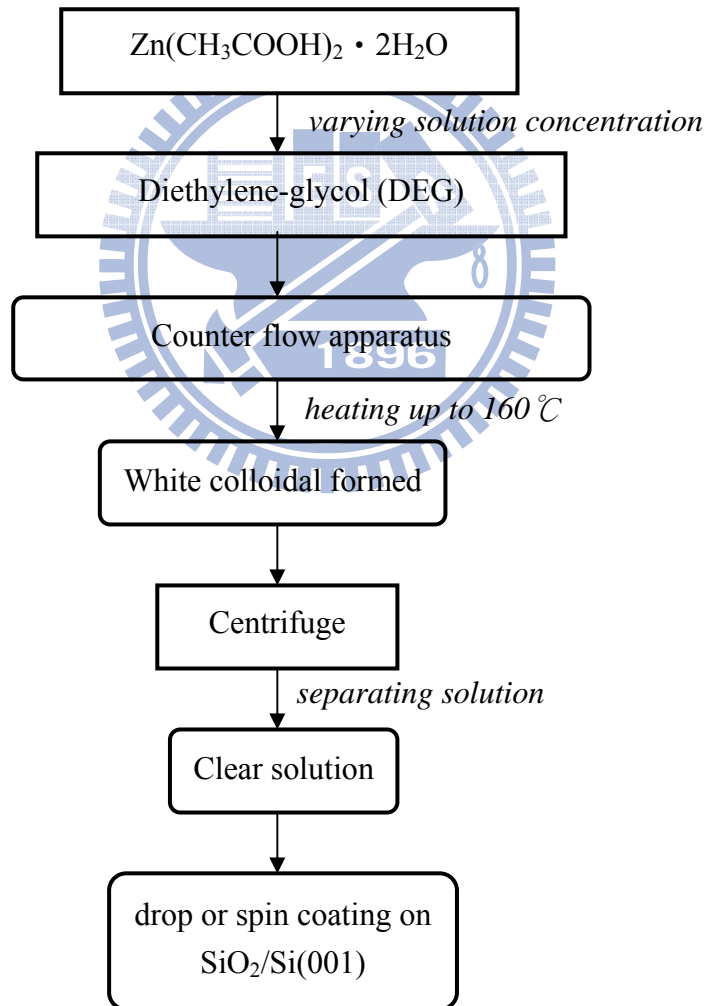Fig. 3-1 Experiment equipment used for fabricating ZnO QDs.



Fig. 3-2 A flow chart of fabricate ZnO QDs by sol-gel method.

## 3.2 Microstructure and optical properties analysis

### 3.2.1 X-ray diffraction

The crystal structures of the as-grown powder were inspected by using XRD (model: MAC Sience, MXP18) at room temperature equipped with CuK X-ray source (λ=1.5405Å) in National Synchrotron Radiation Research Center (NSRRC), Taiwan. Data were recorded between the angle range of 20° < 2θ < 80° with steps of 0.02°and rate of scanning is 40°/min.   The operation voltage of the system is 50 kV and the operation current is 200 mA.   The essential features of x-ray spectrometer are shown in Figure 3-3.   X-rays from the tube *T* are incident on a crystal *C* which may be set at any desired angle to the incident beam by rotation about an axis through *O*, the center of the spectrometer circle.   *D* is a detector which measures the intensity of the diffraction x-rays.
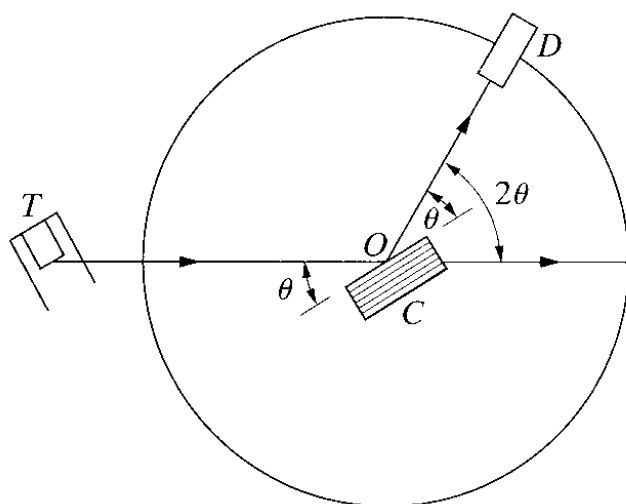


Fig. 3-3 The x-ray spectrometer.

The sizes of the nanocrystallites can be determined by X-ray diffraction using the measurement of the full width at half maximum (FWHM) of the X-ray diffraction lines. The average diameter is obtained by $D = \dfrac{0.89\lambda}{B\cos\theta}$, where D is the average diameter of the nanocrystallite, $\lambda$ is the wavelength of the X-ray source, and B is the FWHM of X-ray diffraction peak at the diffraction angle $\theta$.

### 3.2.2 Photoluminescence system

PL provides a non-destructive technique for the determination of certain impurities in semiconductors. The shallow-level and the deep-level of impurity states were detected by PL system. It was provided radiative recombination events dominate nonradiative recombination.

In the PL measurements, we used a He-Cd cw laser (325 nm) [Kimmon IK5552R-F] as the excitation light. Light emission from the samples was collected into the TRIAX 320 spectrometer and detected by a photomultiplier tube (PMT). As shown in Fig. 3-4, the diagram of PL detection system includes mirror, focusing and collecting lens, the sample holder and the cooling system. The excitation laser beam was directed normally and focused onto the sample surface with power being varied with an optical attenuator. The spot size on the sample is about 100 μm. Spontaneous and stimulated emissions were collected by a fiber bundle and coupled

into a 0.32 cm focal-length monochromator (TRIAX 320) with a 1200 lines/mm

grating, then detected by either an electrically cooled CCD (CCD-3000) or a

photomultiplier tube (PMT-HVPS) detector.   The temperature-dependent PL

measurements were carried out using a closed cycle cryogenic system.   A closed

cycle refrigerator was used to set the temperature anywhere between 15 K and 300 K.

And the power-dependent PL spectra were used for monitoring the characteristic of

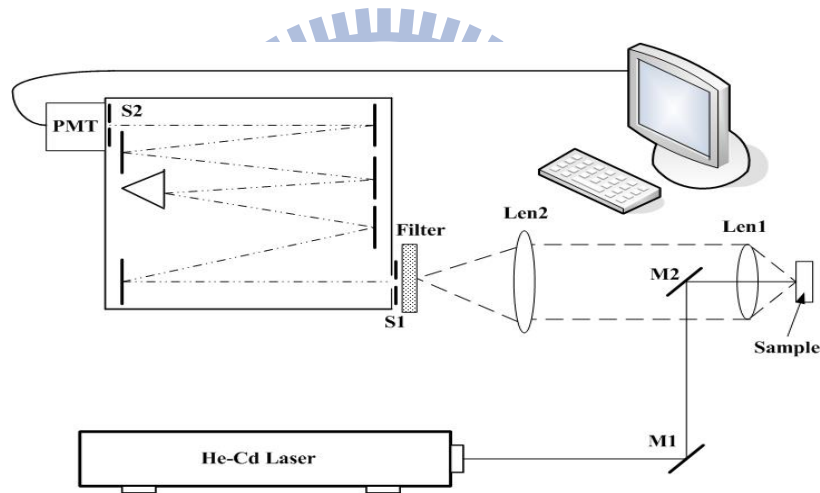excitons and thermalization effect at the different excitation density.



Fig. 3-4 The PL system.

# Chapter 4 Results and Discussion

## 4.1 Morphology and crystal structures

### 4.1.1 Morphology

Shown in Fig. 4-1 is a typical high-resolution transmission electron microscope (HRTEM) image of the ZnO nanoparticles.   Nanoparticles aged at 160 °C for 1 hr and solution concentration of 0.04 M was selected for particle size determination by HRTEM.   The shape of particles is predominantly spherical, and the nanoparticles are clearly well separated and essentially have some aggregation.   The average diameter of the number-weighted particles obtained from a colloid aged at 160 °C for 1 hr (0.04 M) was determined to be $6.18 \pm 0.3$ nm.
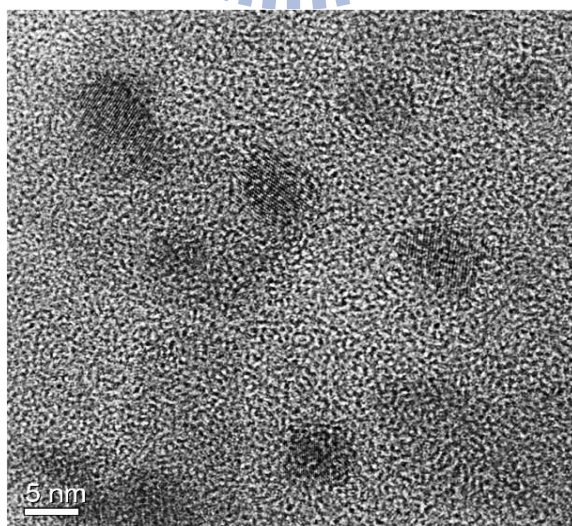


Fig. 4-1 HRTEM image of the ZnO QDs fabricated using 0.04M $Zn(OAc)_2$.

**4.1.2 X-ray diffraction measurement**

The XRD profiles of the ZnO QDs with various concentrations of $Zn(OAc)_2$ are shown in Fig. 4-2. The diffraction pattern and interplanar spacings match nicely with the standard diffraction pattern of wurtzite ZnO, demonstrating the formation of wurtzite ZnO nanocrystals. All of the samples present similar XRD peaks that can be indexed as the wurtzite ZnO crystal structure with lattice constants a = 3.253 Å and c = 5.213 Å, which are consistent with the value in the standard card (JCPDS 89-1397).
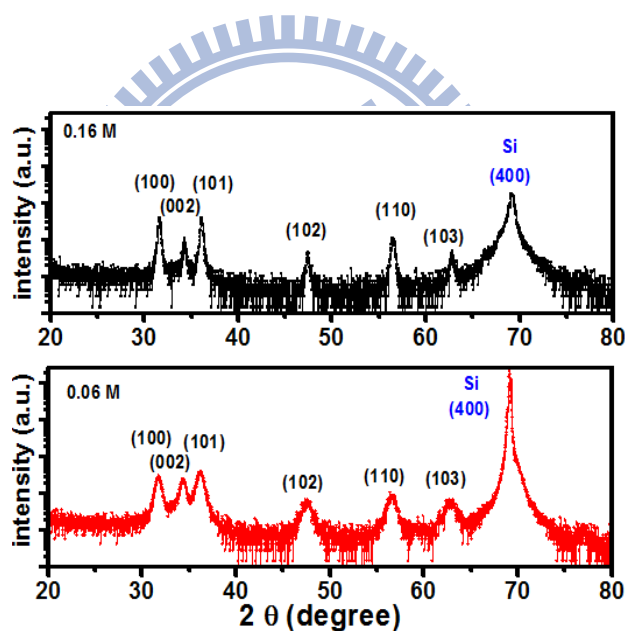


Fig. 4-2 XRD profiles of the ZnO QDs prepared with various concentration of $Zn(OAc)_2$. The crystalline size can be approximately estimated to be 16 and 7 nm, respectively (top to bottom), for concentrations of 0.16 and 0.06 M.

No diffraction peaks of other species could be detected that indicates all the precursors have been completely decomposed and no other crystal products were

formed.   The full width at half maximum (FWHM) of the diffraction peaks increases,

that is, the average crystalline size decreases, as the concentration of zinc precursor

reduces.   The average size is calculated from the width of diffraction peak using the

Debye-Scherer formula: [45, 46] $D = 0.89 \lambda /( w \cos \theta)$, where D is the average

crystalline diameter of the particles, $\lambda$ is the wavelength of the x-ray source, w is the

linewidth at half maximum in excess of the instrumental broadening, and $\theta$ is the

diffraction angle.   The crystalline size can be estimated to be 16 nm and 7 nm, for

concentrations of 0.16 M, and 0.06 M, respectively.

## 4.2 Photoluminescence spectra

### 4.2.1 Photoluminescence spectra for different sizes of ZnO particles

The PL spectra of ZnO QDs with average crystalline sizes of 16 and 7 nm at 13

K are shown in Fig. 4-3.   For the 16-nm ZnO QDs, a strong UV emission peak at

3.388 eV with FWHM of ~ 96 meV was observed accompanied with very broad weak

visible emission with the slightly strong blue emission and rather weak yellow

emission bands.   And only a strong UV emission peak at 3.411 eV with FWHM of ~

174 meV was observed unaccompanied with visible emission for the 7 nm ZnO QDs.

The sharp UV emission peak is attributed to the near band edge emission (NBE) [27,

47].   The broad visible emission is the deep-level emission, which is attributed to the

oxygen vacancy (green emission) or oxygen interstitial (red emission).   The intensity

of the UV and visible peak ratio increases with decreasing the QD size.   The strong

UV emission and weak visible emission in PL spectra indicates that the ZnO QDs
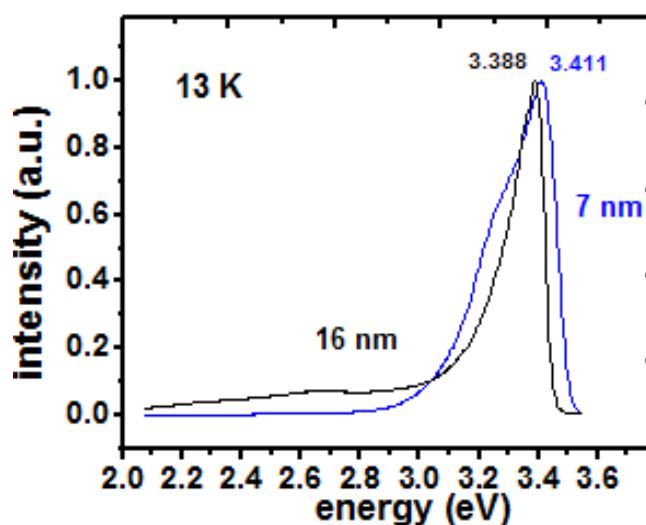
have a good crystal quality.



Fig. 4-3 The PL spectra of the ZnO QDs measured at low temperature.

Figure 4-4 demonstrates the PL spectra of ZnO QDs with different average

crystalline sizes measured at T = 13 K.   The near band edge UV emission is

attributed to the free exciton (FX) emission [32], which shifts (solid line) to the higher

energy (from 3.386 eV to 3.42 eV) as the QD size decreases (16 nm – 6 nm) due to

the quantum confinement effect (QCE).   Besides, the FWHM increases as the

average QDs size decreases that may be caused by the contribution of surface-optical

phonon [48], surface-bound acceptor exciton complexes [25], and size distribution.

Since the Bohr radius of the exciton in bulk ZnO is about 2.34 nm [49], we must

consider the electron hole Coulomb interaction in our samples and the particles are in

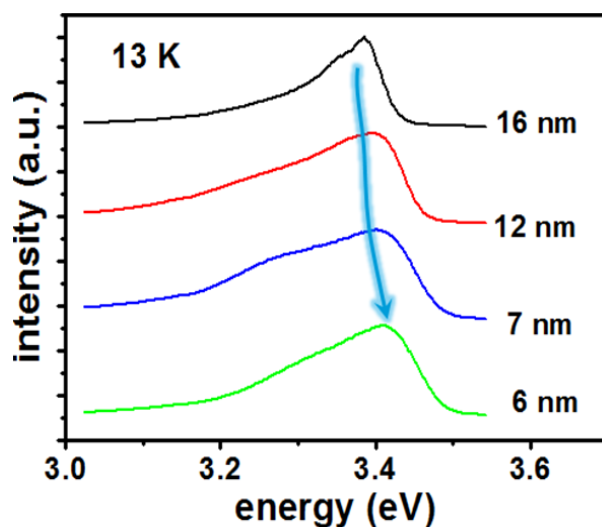the moderate to weak confinement regime.



Fig. 4-4 PL spectra of different sizes of ZnO QD at low temperature. The line indicates the shifts of FX

peak energy.

## 4.2.2 Temperature-dependent PL for different sizes of ZnO particles

Figure 4-5 displays the temperature-dependent PL of different sizes of ZnO, it

reveals only single one band for T = 8 ~ 300 K in QDs system.   Due to small binding

energy of $D_0X$, it will be ionized as T > 100 K, so we can easily attribute the single

band to the FX emission.   We also find that the peak energy difference of FX in QDs

system between 8 K and 300 K decrease with the particle size decreasing.   It is

known that the main contribution to the energy shift is the Fröhlich interaction [50], a

result of Coulomb interaction.
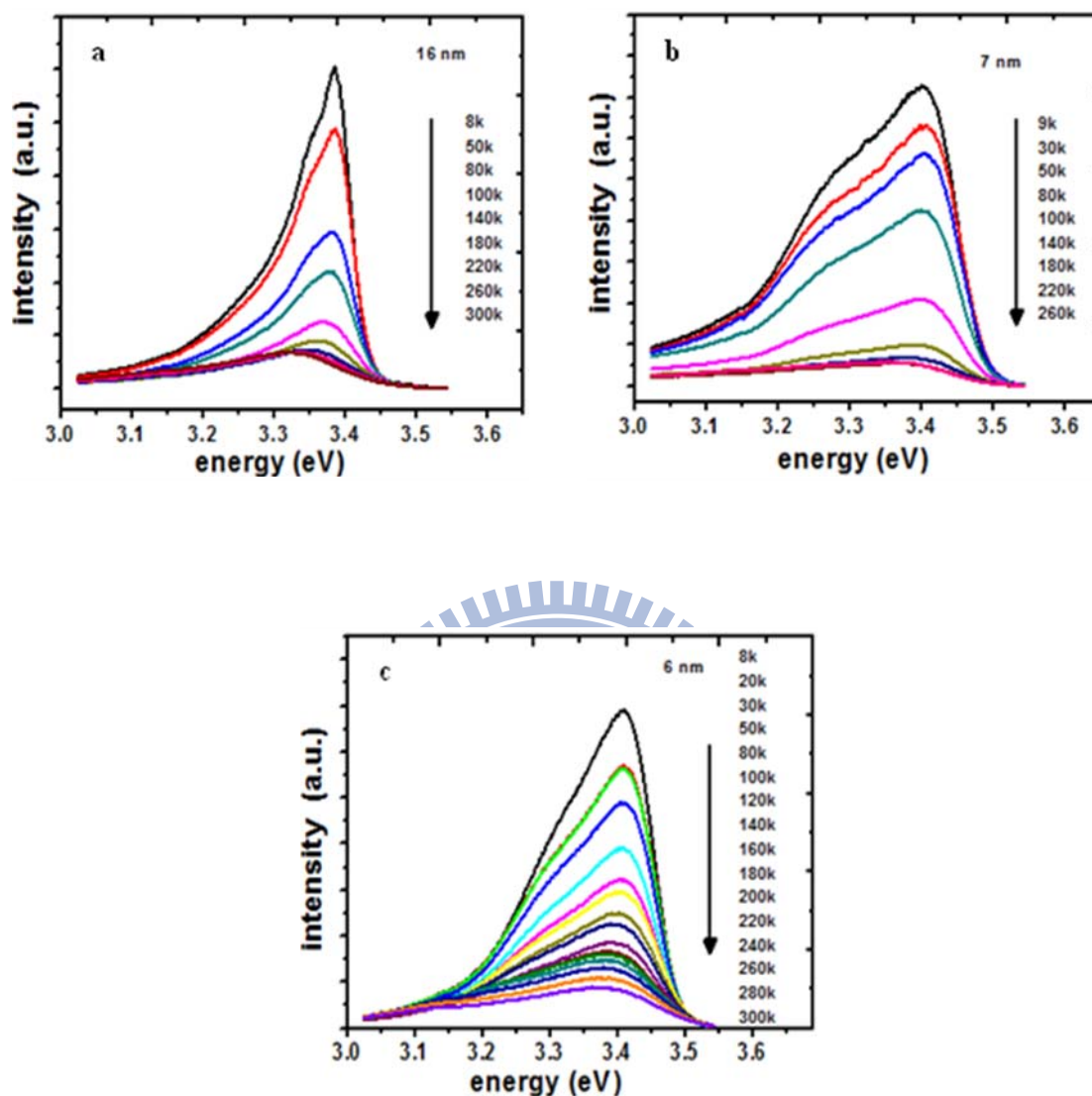


Fig. 4-5 Temperature-dependent PL spectra of (a) 16 nm, (b) 7 nm, (c) 6 nm.

## 4.2.3 Power-dependent PL for different sizes of ZnO particles

The power-dependent PL spectra of different sizes of ZnO QDs are shown in Fig.

4-6. These spectral shapes are almost the same except that the spectral intensity

increases with increasing excitation power from 0.03 mW to 34 mW (43.2 W/cm$^2$ to

49 kW/cm$^2$), covering a range of three orders of magnitude, which show the exciton states remain invariable.

The character in ZnO QDs gives a sharp contrast to the ZnO powder (~ 1 $\mu$m), in which the relative peak intensities of biexciton (BX) and P-band (exciton-exciton scattering) emissions increase as the excitation power increasing [30]. For quantitative analysis, the spectral shape of NBE emission measured in 6-nm ZnO QDs at 80 K is decomposed into two peaks and theoretical fitting results are shown in Fig. 4-7. For comparison, the inset of Fig. 4-7 shows the fit of the PL spectrum in ZnO powder at 80 K. The dashed curves denote the various emissions and the solid curve corresponds to the sum of the theoretical fit, which shows good agreement with the experimental data marked as the open dots. The PL spectra of QDs and that of powder are very diverse. The BX emission can be observed in ZnO powder, nevertheless, in ZnO QDs only the emission of surface bound exciton (SX) [51] rather than BX can be recognized.
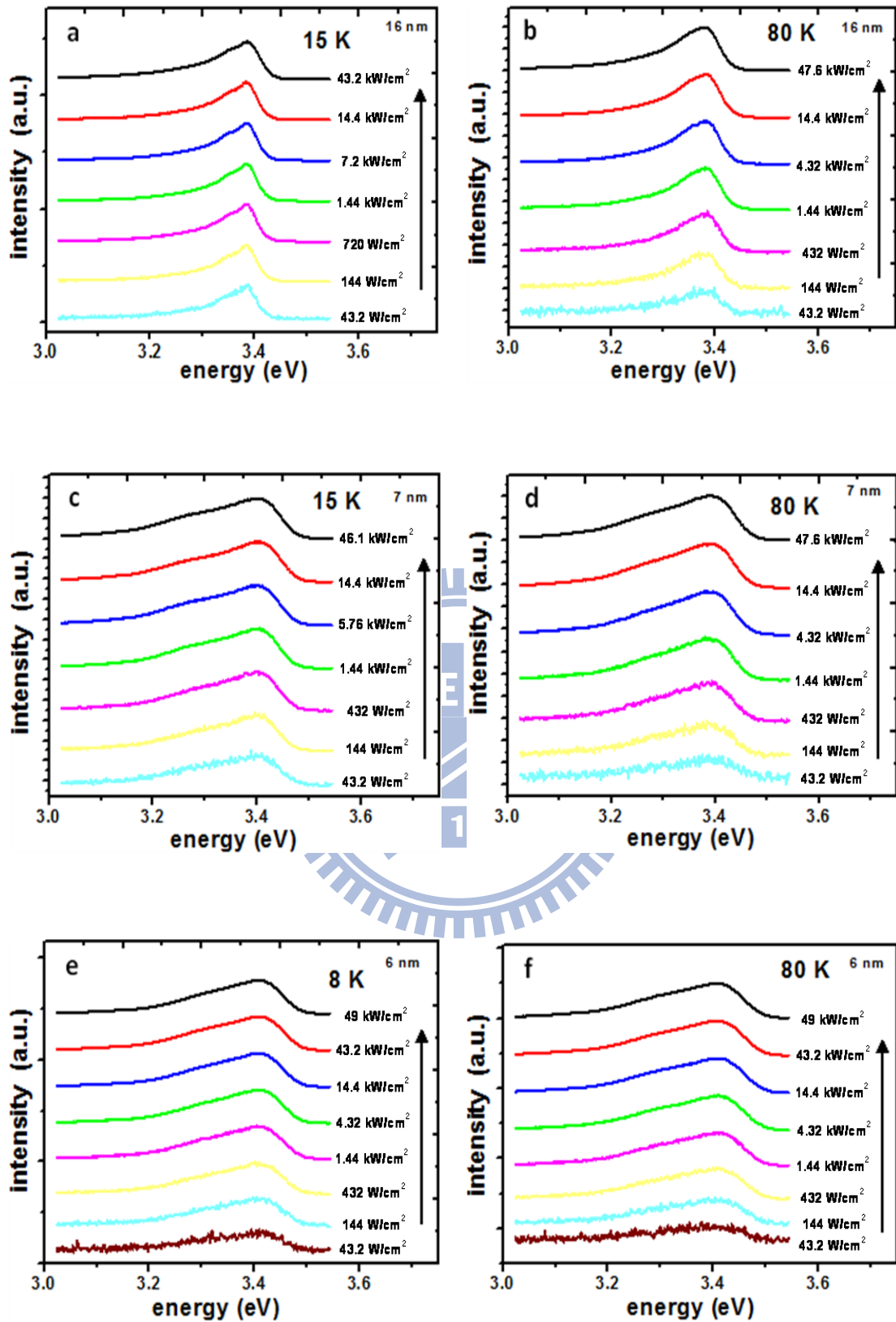
Fig. 4-6 Power-dependent PL spectra of (a) 16 nm at 15 K, (b) 16 nm at 80 K, (c) 7 nm at 15 K, (d) 7 nm at 80 K, (e) 6 nm at 8 K, (f) 6 nm at 80 K.
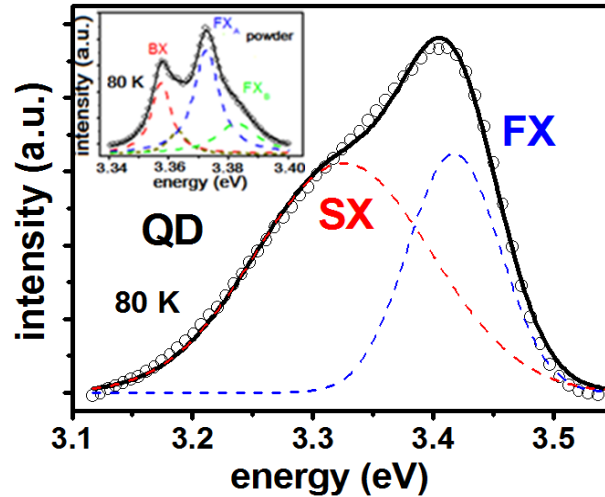
Fig. 4-7 Gaussian fit to a PL spectrum of 6 nm ZnO QDs (0.04M) measured at 80K. The inset shows the spectral fitting for ZnO powder. The fitted line shapes are shown separately in dash lines. Solid lines correspond to the fit and dots represent the data.

## 4.2.4 PL peak positions as a function of excitation power

The peak positions of these emissions with increasing the excitation power in 6-nm ZnO QDs at 80 K are plotted in Fig. 4-8. The FX is observed at 3.418 eV and the PL emission peak at 3.325 eV may be attributed to the emission of SX. The peak positions of FX emission and SX emission are hardly shifted as the excitation power increases from 0.03 to 34 mW.
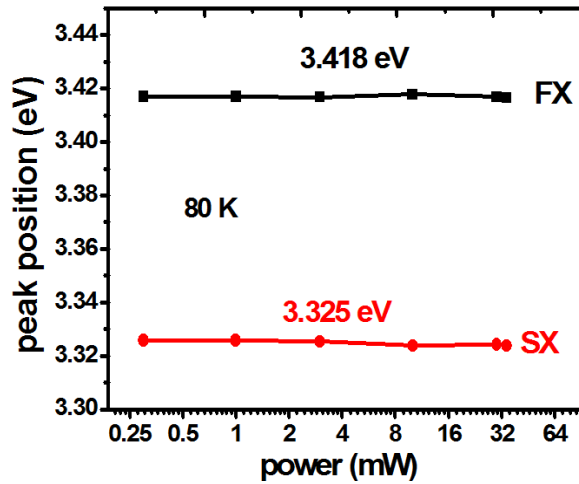
Fig. 4-8 The PL peak positions as a function of excitation power measured at 80K.

### 4.2.5 Integrated intensity as a function of excitation power

In order to further understand the characteristic of these two peaks, the integrated PL intensities of these peaks as a function of excitation power in 6-nm ZnO QDs at 80K are depicted in Fig. 4-9. Both of the integrated intensities exhibit nearly linear dependence on the excitation power with both exponents close to 0.96. However, the exponent of BX (with binding energy of ~15 meV) on the excitation power in ZnO powder comes near the theoretical value of 2 having 1.86 at 80K. It is due to efficient cooling via participation of optical phonons when the exciton kinetic energy approaches to the energy of the lowest optical phonon [30]. However, reducing the exciton-LO phonon coupling in ZnO QDs [32] causes the lack of the efficient cooling of exciton with assistance of optical phonon scattering or the so-called phonon bottleneck. Therefore, it is hardly to allow effectively bounding exciton pairs to form biexcitons in ZnO QDs.

In addition, the P-band emission is hardly found in Fig. 4-6. This finding

means that the probability of exciton-exciton scattering is also very low. For that

reason, we suspect the other reason might be that there is only one exciton existing in

a QD within the exciton lifetime even with the achievable high power CW excitation,

so that neither exciton-exciton scattering nor BX can be observed in ZnO QDs.

Therefore, the increase of excitation intensity provides the larger chance of a single

exciton being excited or the larger excitation rate of single exciton. Thus the peak is

hardly shifted and the PL intensity is linear dependence with excitation intensity

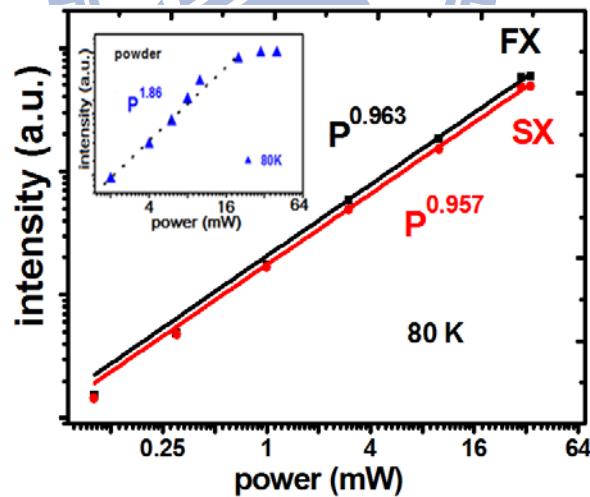corroborating the invariable exciton states upon increasing pumping in ZnO QDs.



Fig. 4-9 The integrated intensity of two decomposed TES and FX peaks as a function of excitation

power measured at 80K. The inset shows the excitation power dependent emission intensity of

biexciton in ZnO powder measured at 80 K. The power factor is 1.86.

# Chapter 5 Conclusions and Prospective

## 5.1 Conclusions

In summary, we have measured XRD to inspect the crystal structures and the average size of ZnO QDs synthesized by a simple sol-gel method. The average sizes of ZnO QDs were verfied by TEM. The diffraction pattern and interplanar spacings indicate the formation of wurtzite ZnO nanocrystals, and no diffraction peaks of other species could be detected that indicates all the precursors have been completely decomposed and no other crystal products were formed. We have measured temperature-dependent and power-dependent PL spectra of ZnO QDs with different sizes to investigate the optical properties. From Size-dependence of efficient UV photoluminescence from low temperature PL gives evidence for quantum confinement effect. The ZnO QDs exhibit strong UV emission and weak visible emission, indicating very good crystal quality. Moreover, the biexciton and P-band emissions in ZnO QDs are hardly observed and unchanged shapes of power-dependent PL spectra show the exciton states remain invariable in ZnO QDs. The intensities of emission peaks associated with these invariable free exciton and surface bound exciton states exhibit linear dependence on the excitation density.

## 5.2 Prospective

In order to further investigate the optical properties of ZnO QDs, we will measure the time resolved photoluminescence (TRPL) to inspect the lifetime of ZnO QDs. Through measuring the lifetime of ZnO QDs, we can identify the different PL origins of physical mechanisms and the process of exciton recombination. Besides, we will do single-photon measurement to study the optical characterizations in a single ZnO QD.

# References

[1]  R. Triboulet, and J. Perriere, Prog. Cryst. Growth Charact. Mater. **47**, 65 (2003).

[2]  U. Ozgur, Y. I. Alivov, C. Liu, A. Teke, M. A. Reshchikov, S. Dogan, V. Avrutin, S. J. Cho, and H. Morkoc, J. Appl. Phys. **98**, 041301 (2005).

[3]  T. Yatsui, J. Lim, M. Ohtsu, S. J. An, and G. C. Yi, Appl. Phys. Lett. **85**, 727 (2004).

[4]  A. B. Djurisic, and Y. H. Leung, Small **2**, 944 (2006).

[5]  A. P. Alivisatos, Science **271**, 933 (1996).

[6]  C. H. Liu, J. A. Zapien, Y. Yao, X. M. Meng, C. S. Lee, S. S. Fan, Y. Lifshitz, and S. T. Lee, Adv. Mater. **15**, 838 (2003).

[7]  B. Liu, and H. C. Zeng, J. Am. Chem. Soc. **125**, 4430 (2003).

[8]  W. I. Park, Y. H. Jun, S. W. Jung, and G. C. Yi, Appl. Phys. Lett. **82**, 964 (2003).

[9]  H. Q. Yan, R. R. He, J. Pham, and P. D. Yang, Adv. Mater. **15**, 402 (2003).

[10] K. F. Lin, H. M. Cheng, H. C. Hsu, L. J. Lin, and W. F. Hsieh, Chem. Phys. Lett. **409**, 208 (2005).

[11] C. J. Pan, K.-F. Lin, W.-T. Hsu, and W.-F. Hsieh, J. Appl. Phys. **102**, 123504 (2007).

[12] J. Y. Lao, J. G. Wen, and Z. F. Ren, Nano Letters **2**, 1287 (2002).

[13] J. Y. Lao, J. Y. Huang, D. Z. Wang, and Z. F. Ren, Nano Letters **3**, 235 (2003).

[14] Y. J. Xing, Z. H. Xi, X. D. Zhang, J. H. Song, R. M. Wang, J. Xu, Z. Q. Xue, and D. P. Yu, Solid State Commun. **129**, 671 (2004).

[15] J. H. Park, H. J. Choi, Y. J. Choi, S. H. Sohn, and J. G. Park, J. Mater. Chem. **14**, 35 (2004).

[16] P. X. Gao, and Z. L. Wang, Appl. Phys. Lett. **84**, 2883 (2004).

[17] X. Y. Kong, and Z. L. Wang, Nano Letters **3**, 1625 (2003).

[18] G. C. Yi, C. R. Wang, and W. I. Park, Semiconductor Science and Technology **20**,

S22 (2005).

[19] L. E. Brus, J. Chem. Phys. **80**, 4403 (1984).

[20] L. T. Canham, Appl. Phys. Lett. **57**, 1046 (1990).

[21] Y. Kayanuma, Phys. Rev. B **38**, 9797 (1988).

[22] J. B. Xia, and K. W. Cheah, Phys. Rev. B **59**, 14876 (1999).

[23] L. Guo, S. H. Yang, C. L. Yang, P. Yu, J. N. Wang, W. K. Ge, and G. K. L. Wong, Appl. Phys. Lett. **76**, 2901 (2000).

[24] N. Pan, X. P. Wang, M. Li, F. Q. Li, and J. G. Hou, J. Phys. Chem. C **111**, 17265 (2007).

[25] V. A. Fonoberov, and A. A. Balandin, Appl. Phys. Lett. **85**, 5971 (2004).

[26] B. P. Zhang, N. T. Binh, Y. Segawa, K. Wakatsuki, and N. Usami, Appl. Phys. Lett. **83**, 1635 (2003).

[27] B. P. Zhang, N. T. Binh, Y. Segawa, Y. Kashiwaba, and K. Haga, Appl. Phys. Lett. **84**, 586 (2004).

[28] S. W. Kim, and S. Fujita, Appl. Phys. Lett. **86**, 153119 (2005).

[29] X. Q. Zhang, Z. G. Yao, S. H. Huang, I. Suemune, and H. Kumano, J. Appl. Phys. **99**, 063709 (2006).

[30] C. J. Pan, K. F. Lin, and W. F. Hsieh, Appl. Phys. Lett. **91**, 111907 (2007).

[31] S. Y. Kim, Y. S. Yeon, S. M. Park, J. H. Kim, and J. K. Song, Chem. Phys. Lett. **462**, 100 (2008).

[32] W. T. Hsu, K. F. Lin, and W. F. Hsieh, Appl. Phys. Lett. **91**, 181913 (2007).

[33] D. M. Bagnall, Y. F. Chen, Z. Zhu, T. Yao, M. Y. Shen, and T. Goto, Appl. Phys. Lett. **73**, 1038 (1998).

[34] C. J. Brinker, and G. W. Scherer, *Sol-Gel Sience* (Academic Press, 1990), p. 303.

[35] C. F. Klingshirn, *Semiconductor Optics* (Springer, 1997).

[36] S.-B. Yin, in *National Chiao Tung University Department of Photonics* (National

Chiao Tung University, 1999).

[37] J. Singh, *Physics of Semiconductors and Their Heterostructures* (McGraw-Hill, Singapore, 1993), p. 17&316.

[38] B. D. Cullity, *Element of X-ray diffraction* (Addison Wesley, Canada, 1978).

[39] A. Taylor, *X-ray Metallography* (John Wiley and Sons, New York, 1961), p. 676.

[40] F. Mark, *Optical Properties of Solids* (Oxfrd university press, 2001).

[41] S. Perlpwotz, *Optical characterization of semiconductors: infaraed, Raman, and Photoluminescence spectroscopy* (Academic Press, London, 1993).

[42] A. Teke, U. Ozgur, S. Dogan, X. Gu, H. Morkoc, B. Nemeth, J. Nause, and H. O. Everitt, Phys. Rev. B **70**, 195207 (2004).

[43] H. Alves, D. Pfisterer, A. Zeuner, T. Riemann, J. Christen, D. M. Hofmann, and B. K. Meyer, Optical Materials **23**, 33 (2003).

[44] J. B. Baxter, and E. S. Aydil, Appl. Phys. Lett. **86**, 053114 (2005).

[45] E. F. Kaelble, *Handbook of X-rays* (McGraw-Hill, New York, 1967).

[46] J. C. Bailar, A. F. Trotman-Dickenson, H. J. Emeleus, and S. R. Nyholm, *Comprehensive Inorganic Chemistry* (Pergamon, Oxford, 1973), Vol. 3.

[47] H. C. Hsu, Y. K. Tseng, H. M. Cheng, J. H. Kuo, and W. F. Hsieh, J. Crystal Growth **261**, 520 (2004).

[48] Z. D. Fu, Y. S. Cui, S. Y. Zhang, J. Chen, D. P. Yu, S. L. Zhang, L. Niu, and J. Z. Jiang, Appl. Phys. Lett. **90**, 263113 (2007).

[49] R. T. Senger, and K. K. Bajaj, Phys. Rev. B **68**, 045313 (2003).

[50] S. J. Sheih, K. T. Tsen, D. K. Ferry, A. Botchkarev, B. Sverdlov, A. Salvador, and H. Morkoc, Appl. Phys. Lett. **67**, 1757 (1995).

[51] V. A. Fonoberov, K. A. Alim, A. A. Balandin, F. X. Xiu, and J. L. Liu, Phys. Rev. B **73** (2006).